Sensors and Materials, Vol. 38, No. 10 (2026) 6323–6334
MYU Tokyo

S & M 4683

Effects of Processing Parameters on Thermoelectric Properties of n-Type $Bi_2Te_{2.3}Se_{0.7}$ Thermoelectric Materials

Yin-Chen Huang,[1] Ping-Chen Lin,[2] and Tao-Hsing Chen[2*]

[1]Institute for Materials Research, Tohoku University, 2-1-1, Katahira, Aoba-ku, Sendai 980-8577, Japan
[2]Department of Mechanical Engineering, National Kaohsiung University of Science and Technology, No. 415, Jiangong Rd., Sanmin Dist., Kaohsiung City 807618, Taiwan

(Received August 30, 2026; accepted October 21, 2026)

Keywords: thermoelectric sensors, spark plasma sintering, processing parameters, figure of merit, ball milling, vacuum-induced melting

In this study, the effects of different powder metallurgy processing routes on the thermoelectric properties of n-type $Bi_2Te_{2.3}Se_{0.7}$ alloys were systematically investigated. Three powder metallurgy processes were used in this study: (A) ball milling followed by spark plasma sintering (SPS), (B) ball milling combined with vacuum induction melting (VIM) prior to SPS, and (C) ball milling – VIM – ball milling and finally SPS. The effect of an SPS pressure of 50 MPa on the thermoelectric performance was also evaluated. Among all the processing conditions, Process A combined with an SPS pressure of 50 MPa resulted in the highest thermoelectric performance. This processing route effectively preserved continuous carrier transport pathways while maintaining abundant grain boundaries and fine microstructural features, thereby enhancing phonon scattering and suppressing lattice thermal conductivity to approximately 0.45 $W \cdot m^{-1} \cdot K^{-1}$ at 390 K. Consequently, the highest dimensionless figure of merit ($ZT \approx 0.81$) was achieved at 390 K. These results demonstrate that optimizing the balance between electrical and thermal conductivities through appropriate processing parameters is critical for maximizing the thermoelectric efficiency of n-type $Bi_2Te_{2.3}Se_{0.7}$ alloys.

1. Introduction

The increasing demand for sustainable energy technologies and the urgent need to improve energy utilization efficiency have stimulated extensive research on waste heat recovery systems. A considerable proportion of the energy generated in industrial manufacturing, transportation, and electronic devices is inevitably dissipated as waste heat. The direct conversion of this thermal energy into electrical energy provides an attractive approach for improving overall energy efficiency while reducing fossil fuel consumption and greenhouse gas emissions. Among various energy conversion technologies, the use of thermoelectric (TE) materials has attracted significant attention because TE materials can directly convert heat into electricity through the Seebeck effect without involving moving parts, working fluids, or complex mechanical

*Corresponding author: e-mail: thchen@nkust.edu.tw
https://doi.org/10.18494/SAM6601

ISSN 0914-4935 © MYU K.K.
https://myukk.org/

systems.[1–6] Consequently, TE power generation has been recognized as one of the most promising technologies for harvesting low-grade waste heat.

Among commercially available TE materials, Bi_2Te_3-based alloys exhibit the highest TE performance within the low-temperature range of approximately 300–500 K. Owing to their excellent electrical transport characteristics and relatively low thermal conductivity, Bi_2Te_3-based compounds have become dominant materials for room-temperature TE power generation and solid-state refrigeration. Practical TE modules generally consist of p-type and n-type semiconductor legs connected electrically in series and thermally in parallel. Therefore, improving the TE performance of both p-type and n-type Bi_2Te_3-based materials is essential for enhancing the overall conversion efficiency of TE devices.[7–10]

The TE efficiency of a material is commonly evaluated by the dimensionless figure of merit, *ZT*, which is expressed as[11–13]

$$ZT = S^2 \cdot \sigma \cdot T \cdot \kappa^{-1}, \tag{1}$$

where S is the Seebeck coefficient, σ is the electrical conductivity, κ is the total thermal conductivity, and T is the absolute temperature. Because these transport parameters are strongly coupled, improving one parameter often leads to the deterioration of another. Consequently, achieving high TE performance requires simultaneously enhancing electrical transport while suppressing thermal conductivity, representing one of the major challenges in TE material design.

Although numerous studies have investigated ball milling, induction melting, and spark plasma sintering (SPS) individually, a comprehensive comparison of their combined processing routes for n-type $Bi_2Te_{2.3}Se_{0.7}$ alloys remains limited. In particular, the synergistic effects of ball milling, induction melting, secondary ball milling, and SPS pressure on the evolution of microstructure and TE transport behavior have not yet been fully clarified.[14,15]

Therefore, in this study, we systematically investigated the effects of different powder metallurgy processing routes on the TE properties of n-type $Bi_2Te_{2.3}Se_{0.7}$ alloys. Three fabrication routes were designed, namely, (A) conventional ball milling followed by SPS, (B) ball milling combined with vacuum induction melting (VIM) before SPS, and (C) induction melting followed by secondary ball milling prior to SPS. The effect of an SPS pressure of 50 MPa was also evaluated. The resulting phase constitution, microstructure, elemental distribution, electrical conductivity, Seebeck coefficient, thermal conductivity, power factor, and dimensionless figure of merit (*ZT*) were systematically characterized to establish the processing–microstructure–property relationship. The findings of this work provide useful guidelines for optimizing processing parameters and developing high-performance BiTe-based TE materials for low-temperature energy conversion applications.[16,17]

2. Materials and Methods

Commercial high-purity elemental powders of bismuth (Bi), tellurium (Te), and selenium (Se) were employed as the materials for preparing the n-type $Bi_2Te_{2.3}Se_{0.7}$ TE materials. These elemental powders were weighed according to the designed stoichiometric ratio before subsequent powder processing. Different fabrication processes were employed to synthesize the TE materials. The detailed descriptions of each process are as follows:

- Process A: The blended elemental powders were mechanically alloyed using a high-energy ball mill for 1 h, followed by SPS (use Se A in Fig. 1).
- Process B: After ball milling, the alloy powders were subjected to VIM at 600 °C to improve alloy homogeneity and promote chemical mixing. The solidified alloy was then consolidated by SPS (use Se B in Fig. 1).
- Process C: The ingots were ball-milled and subjected to VIM. Then, the ingots were ball-milled again before being subjected to SPS consolidation. The additional milling treatment was intended to refine the particle size, increase the grain-boundary density, and enhance phonon scattering (use Se C in Fig. 1).

The consolidation pressure of 50 MPa was employed to investigate its effects on densification and TE transport behavior. After sintering, all specimens were ground, polished, and machined

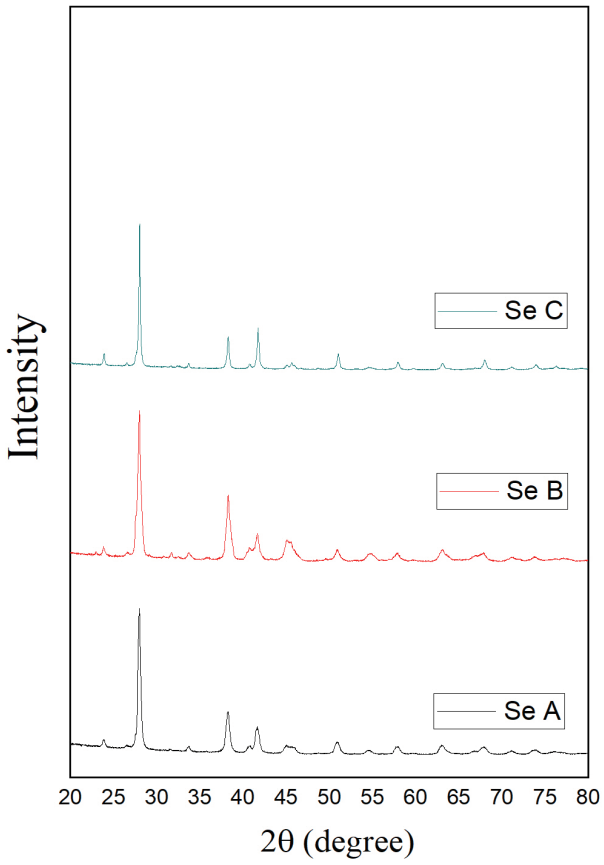


Fig. 1. (Color online) XRD analysis results of n-type $Bi_2Te_{2.3}Se_{0.7}$ alloys under different processing routes.

into the required dimensions for subsequent characterization and TE measurements. Planetary ball milling was conducted at a rotational speed of 350 rpm for 1 h. The VIM process involved melting at 600 °C for 10 min and cooling under vacuum for 30 min. Ingots with a diameter of 15 mm and a thickness of 7–8 mm were then obtained.

To verify the alloy composition and phase structure, the samples were first examined using an energy-dispersive X-ray spectrometer to confirm the added elements, followed by structural analysis using an X-ray diffraction (XRD) system (Bruker D8). The ingot surfaces were polished to remove oxides, and the samples were cut into rectangular bars with dimensions of approximately $2 \times 2 \times 7$ mm^3 using a low-speed cutter for property measurements. The temperature-dependent TE transport properties were measured using a physical property measurement system (PPMS) to measure the Seebeck coefficient, electrical conductivity, and power factor in the temperature range of 300–400 K.

3. Results and Discussion

3.1 Phase analysis by XRD

To obtain the excellent fabrication process while maintaining experimental efficiency, the effect of ball-milling duration on phase formation was first investigated. Figure 2 shows the XRD patterns of $Bi_2Te_{2.3}Se_{0.7}$ powders milled for durations ranging from 1 to 6 h. Compared with the standard JCPDS, all n-type samples exhibited diffraction peaks consistent with the reference pattern, and no clear impurity phases were detected. Increasing the milling time up to 6 h produced no notable peak shift or additional impurity phases, suggesting that prolonged milling did not significantly change the crystal structure. The milling time of 1 h was selected as the optimum processing parameter for all subsequent experiments. Figure 1 illustrates the XRD patterns of the n-type $Bi_2Te_{2.3}Se_{0.7}$ alloys fabricated using three different processing routes. The XRD analysis demonstrates that all three processing routes successfully synthesized high-purity rhombohedral $Bi_2Te_{2.3}Se_{0.7}$ without detectable oxide phases or residual reactants, confirming that the combined VIM and protected ball-milling processes effectively preserved the chemical stability of the Bi–Te–Se system throughout fabrication. Although the samples of Process A exhibited relatively low crystallinity, their refined grain structure and high lattice strain are advantageous for enhancing phonon scattering, thereby suppressing lattice thermal conductivity. Consequently, this processing route provides significant microstructural advantages for achieving low thermal conductivity.

The pronounced enhancement of the (10 10) diffraction peak in the samples of Process B indicates that induction melting effectively induced the preferred orientation during solidification. Considering the highly anisotropic transport behavior of Bi_2Te_3-based TE materials, such crystallographic texture is expected to affect the carrier mobility and consequently improve the electrical transport performance.

The specimens of Process C also had the high crystallinity peak owing to the thermo-mechanical cycle consisting of induction melting followed by secondary ball milling. The improved chemical homogeneity and reduced lattice strain produced the most structurally stable material among all processing routes, which is expected to facilitate efficient carrier transport

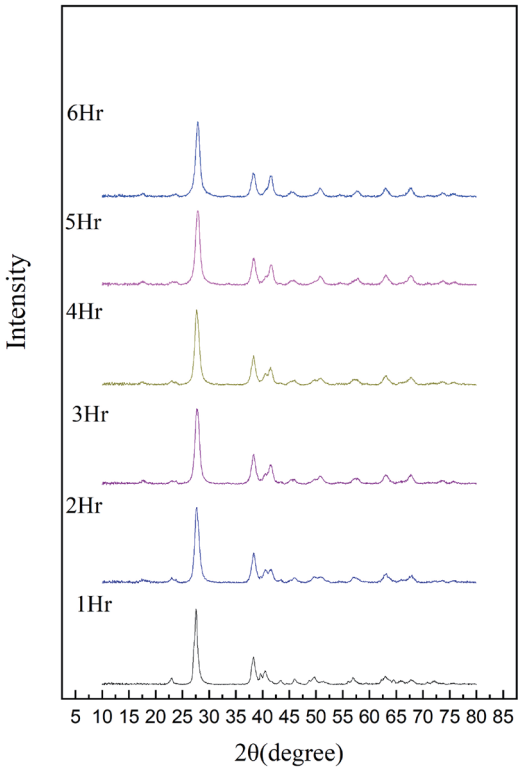


Fig. 2. (Color online) XRD analysis of n-type $Bi_2Te_{2.3}Se_{0.7}$ alloys under different ball milling times.

3.2 Conductivity analysis

As shown in Fig. 3, the electrical conductivities of all the specimens decrease slightly with increasing temperature. Among the bulk samples, the specimens of Process A achieved the highest conductivity at 6×10^4 S·m^{-1} at 300 K, suggesting that the ball milling processes improve the crystal structure and carrier concentration. The specimens that used the vacuum-induced melting process had low conductivity. Previous studies demonstrated that that Bi_2Te_3-based alloys are particularly vulnerable to the volatilization of Te and Se during high-temperature processing, which induces non-stoichiometric defects, including vacancies and antisite defects.[18] In this work, repeated high-temperature exposure during high-frequency processing is expected to accelerate the evaporation of volatile chalcogen elements, resulting in compositional deviations from the ideal stoichiometry. Such defect formation not only enhances carrier scattering but also perturbs the electronic band structure and carrier concentration. Consequently, the carrier mobility significantly decreases, leading to the observed deterioration in the electrical transport properties of all samples. Figure 4 shows the electrical resistivity of all the samples, displaying the inverse trend of the electrical conductivity

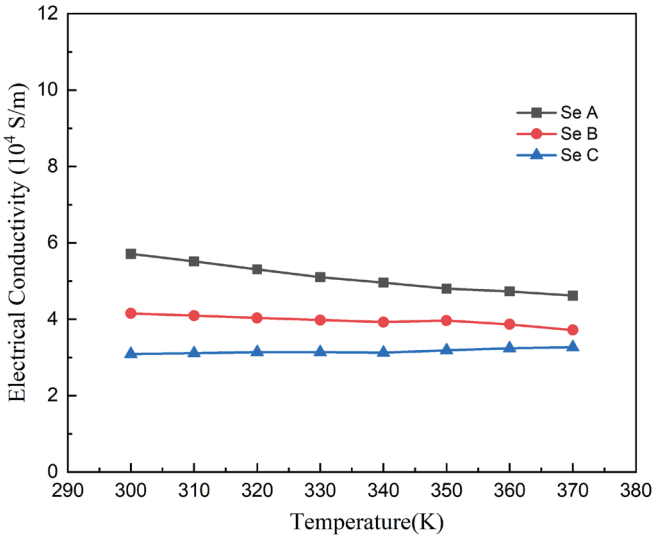


Fig. 3. (Color online) Relationship of conductivity and temperature for n-type $Bi_2Te_{2.3}Se_{0.7}$ alloys.

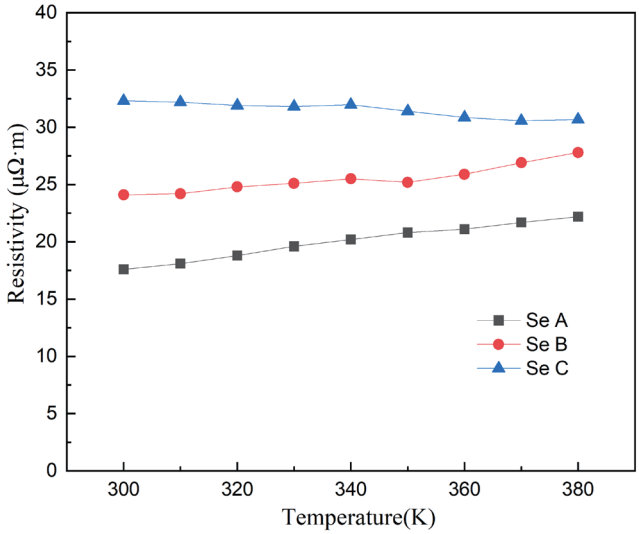


Fig. 4. (Color online) Relationship of resistivity and temperature for n-type $Bi_2Te_{2.3}Se_{0.7}$ alloys.

3.3 Seebeck coefficient analysis

As shown in Fig. 5, all the specimens exhibit a similar temperature-dependent evolution of $|S|$, although notable differences in magnitude are observed among the various processing conditions. These differences suggest that processing-induced variations in microstructure and

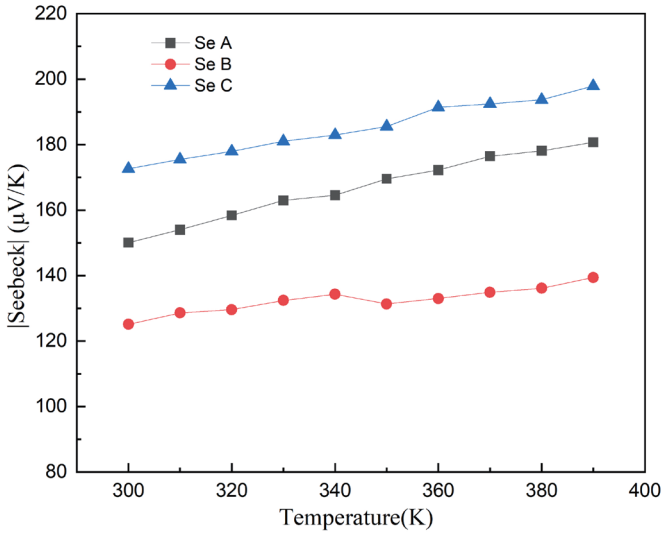


Fig. 5. (Color online) Seebeck coefficient of n-type n-type $Bi_2Te_{2.3}Se_{0.7}$ versus temperature.

composition alter the carrier transport characteristics, thereby affecting the TE performance. As shown in Fig. 5, the absolute Seebeck coefficient ($|S|$) of all the specimens gradually increases with temperature, which is characteristic of heavily doped (degenerate) Bi_2Te_3-based semiconductors.[19] As the temperature increases, the average energy transported by charge carriers increases, resulting in an enhanced TE potential and, consequently, a higher Seebeck coefficient. Note that the Process C specimen, despite exhibiting the lowest electrical conductivity, showed the highest absolute Seebeck coefficient, reaching nearly 200 μV/K at 390 K. The reduced electrical conductivity of the Process C specimen is likely associated with a lower carrier concentration, resulting in a higher average carrier transport energy and consequently an enhanced Seebeck coefficient. Nevertheless, a larger Seebeck coefficient does not necessarily translate into superior TE performance, as the substantial reduction in electrical conductivity may offset its contribution to the power factor.

3.4 Power factor analysis

The specimens consolidated under a sintering pressure of 50 MPa with prior high-frequency induction melting at 600 °C (Processes B and C) exhibited consistently lower power factor values over the entire measured temperature range than the ball-milled reference specimen (Process A). This trend is consistent with the deterioration in electrical conductivity discussed previously, indicating that the reduction in electrical transport predominantly governs the overall power factor. The explanation is that the high-temperature induction melting treatment promoted the partial volatilization of high-vapor-pressure constituents, such as Te and Se, resulting in deviations from the nominal stoichiometric composition. The associated formation of vacancies and point defects increased carrier scattering within the crystal lattice, thereby reducing the

carrier mobility and suppressing the long-range charge transport. Consequently, although the Seebeck coefficient was partially enhanced, the reduction in electrical conductivity outweighed this benefit, ultimately limiting the improvement in power factor. Figure 6 shows the power factors of $Bi_2Te_{2.3}Se_{0.7}$ [see Eq. (2)].[20,21] For all the samples, the power factor increased with temperature. Among them, the specimen of Process A exhibited the highest power factor, reaching approximately 14.8×10^{-4} W/m·K^2 at 380 K. This superior performance is attributed to its relatively high electrical conductivity and favorable Seebeck coefficient. The ball-milled $Bi_2Te_{2.3}Se_{0.7}$ sample demonstrated a substantial improvement in power factor compared with its bulk counterpart, maintaining higher values across the entire temperature range.

$$PF = S^2\sigma \tag{2}$$

3.5 Thermal conductivity analysis and figure of merit (*ZT* value)

Figure 7 shows the thermal conductivity of n-type $Bi_2Te_{2.3}Se_{0.7}$. We used the PPMS system to measure the thermal conductivity. The thermal conductivities of Process B and C samples increased with temperature. However, the thermal conductivities of Process A samples decreased with increasing temperatures. Among the bulk samples, Process A samples had the lowest value of 0.45 W/m·K at 390 K. In contrast, Process B and C samples exhibited significantly higher thermal conductivities than Process A samples across the entire temperature range. Figure 8 shows the dimensionless figure of merit of n-type $Bi_2Te_{2.3}Se_{0.7}$ [*ZT*, see Eq. (1)].[22–24]

For all the samples, *ZT* increased with temperature. Among the bulk samples, the Process A sample achieved the highest *ZT* of 0.81 at 390 K owing to its relatively high electrical conductivity, favorable Seebeck coefficient, and lowest thermal conductivity.

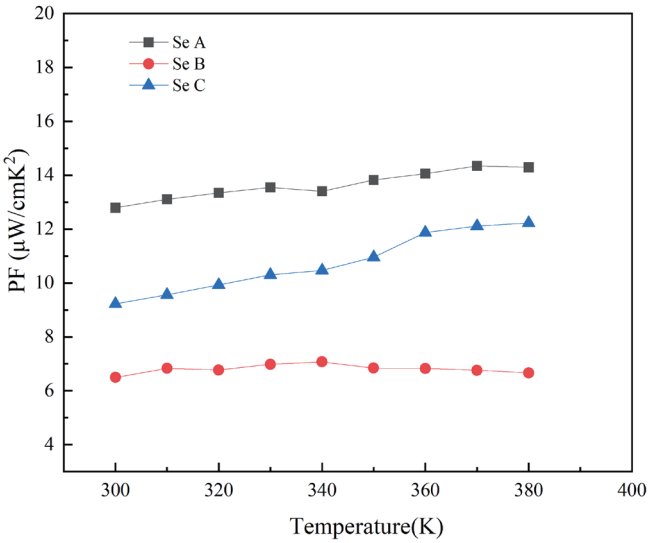


Fig. 6. (Color online) n-type $Bi_2Te_{2.3}Se_{0.7}$ power factor versus temperature.

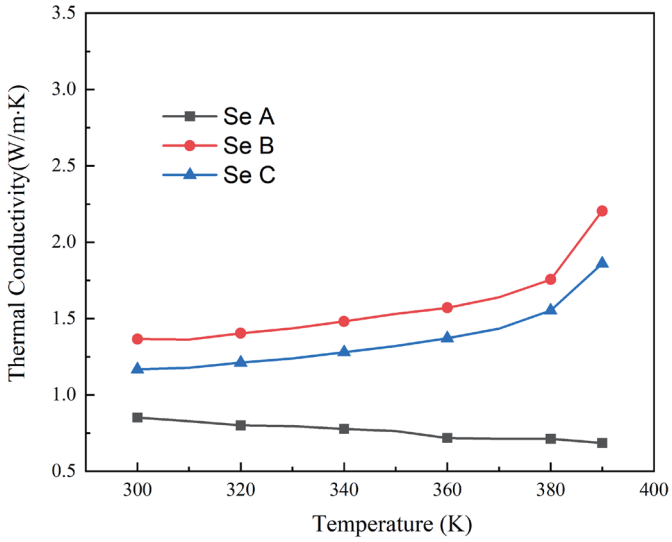


Fig. 7. (Color online) Thermal conductivity versus temperature for n-type $Bi_2Te_{2.3}Se_{0.7}$.

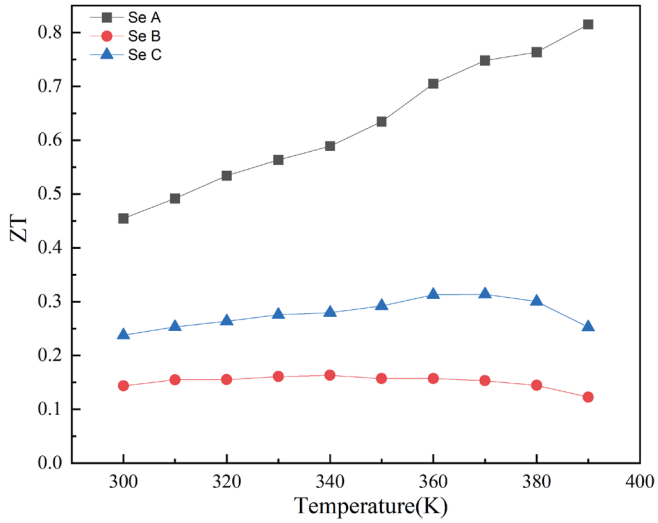


Fig. 8. (Color online) n-type $Bi_2Te_{2.3}Se_{0.7}$ *ZT* versus temperature.

4. Conclusions

In this study, we systematically investigated the effects of processing routes (Processes A–C) and sintering pressure (50 MPa) on the microstructural evolution and temperature-dependent TE transport properties of the n-type $Bi_2Te_{2.3}Se_{0.7}$ solid solution. Under the relatively low sintering

pressure of 50 MPa, the samples subjected to high-temperature high-frequency induction melting (Se B and Se C) exhibited a pronounced increase in electrical resistivity over the investigated temperature range. Although the induction-melting treatment may promote microstructural and crystallographic orientation changes, exposure to elevated temperatures can also facilitate the volatilization of low-melting-point elements with relatively high vapor pressures, particularly Te and Se. In contrast, the Se A sample, fabricated without the high-frequency induction-melting treatment and sintered at 50 MPa, exhibited the most favorable balance between electrical and thermal transport properties. The moderately porous microstructure and abundant grain-boundary interfaces provided effective phonon-scattering sites across multiple characteristic length scales. Consequently, the total thermal conductivity was suppressed to approximately 0.45 W m^{-1} K^{-1} at 390 K throughout the investigated temperature range. Importantly, this reduction in thermal conductivity was achieved without severely deteriorating the electrical transport properties, resulting in an advantageous balance among electrical conductivity, Seebeck coefficient, and thermal conductivity.

As a result, the Se A sample achieved the highest ZT, with a maximum of approximately 0.81 at 390 K. These results demonstrate that minimizing the volatilization-induced degradation of electrical transport while introducing an appropriate degree of microstructural phonon scattering is more effective than simply increasing processing complexity. The present findings therefore provide useful guidance for optimizing the processing conditions of n-type $Bi_2Te_{2.3}Se_{0.7}$ TE materials for low-temperature TE applications.

Acknowledgments

This study was completed through Research Projects NSTC 115-2221-E-992 -032 -MY3 and 115-2637-E-992 -002, which are supported by the National Science and Technology Council of Taiwan. This work was also supported by the Frontier Metal Forming Research and Development Center of Taiwan. The authors also gratefully acknowledge the use of EM000700 and XRD003100 of NSTC 115-2740-M-006-001 belonging to the Core Facility Center of National Cheng Kung University.

References

1 G. J. Snyder and E. S. Toberer : Nat. Mater. **7** (2008) 105. https://doi.org/10.1038/nmat2090
2 H. J. Goldsmid: Materials **7** (2014) 2577. https://doi.org/10.3390/ma7042577
3 K. Kawajiri, Y. Kishita, and Y. Shinohara: Sustainability **13** (2021) 13630. https://doi.org/10.3390/su132413630
4 Q. Li, Z. Wei, Q. Ma, Z. Li, and J. Luo: ACS Omega **6** (2021) 33883. https://doi.org/10.1063/1.4976125
5 T. H. Chen, S. A. Tsai, and T. Y. Zeng: Sens. Mater. **29** (2017) 1637. https://doi.org/10.18494/SAM.2017.1737
6 T. H. Chen and M. T. Hong: Sens. Mater. **28** (2017) 503. https://doi.org/10.18494/SAM.2016.1306
7 L.Yang, Z.-G. Chen, M. Hong, G. Han, and J. Zou, ACS Appl. Mater. Interfaces **7** (2015) 23694. https://doi.org/10.1021/acsami.5b07596
8 Y. Wang, W. D. Liu, H. Gao, L. J. Wang, M. Li, X. L. Shi, M. Hong, H. Wang, J. Zou, and Z. G. Chen: ACS Appl. Mater. Interfaces **11** (2019) 31237. https://doi.org/10.1021/acsami.9b12079
9 X. L. Shi, J. Zou, and Z. G. Chen: Chem. Rev. **120** (2020) 7399. https://doi.org/10.1021/acs.chemrev.0c00026
10 Y.C. Shih, J..F. Lin, S. C. Shi, and G. Y. Chen: Sens. Mater. **37** (2025) 1881. https://doi.org/10.18494/SAM5517
11 H. Ohta, S. Kim, Y. Mune, T. Mizoguchi, K. Nomura, S. Ohta, T. Nomura, Y. Nakanishi, Y. Ikuhara, M. Hirano, H. Hosono, and K. Koumoto: Nat. Mater. **6** (2007) 129. https://doi.org/10.1038/nmat1821

12 C. Hu, Z. Gao, M. Zhang, S. Han, C. Fu, and T. Zhu: Energy Environ. Sci. **16** (2023) 5381. https://doi.org/10.1039/d3ee02167j
13 F. Guo, Y. Sun, H. Qin, Y. Zhu, Z. Ge, Z. Liu, W. Cai, and J. Sui: Scri. Mater. **218** (2022) 114801. https://doi.org/10.1016/j.scriptamat.2022.114801
14 D. Rahmadiawan, W.-H. Lin, J. F. Lin, S.C. Shi, T.-H. Chen, and H. T. Lin: ACS Omega (2026). https://doi.org/10.1021/acsomega.5c12125
15 K. Zhou, J. Chen, R. Zheng, X. Ke, T. Zhang, X. Shi, and L. Chen: Ceram. Int. **42** (2016) 12490. https://doi.org/10.1016/j.ceramint.2016.05.037
16 Y. Liu, M. Zhou, and J. He: Scr. Mater. **111** (2016) 39. https://doi.org/10.1016/j.scriptamat.2015.06.031.
17 Y. Pan, T.-R. Wei, Q. Cao, and J.-F Li: Mater. Sci. Eng. B **197** (2015) 75. https://doi.org/10.1016/j.mseb.2015.03.011.
18 Y. Wang, W.-D. Liu, X. L. Shi, M. Hong, L.-J. Wang, M. Li, H. Wang, J. Zou, and Z. G. Chen: Chem. Eng. J. **391** (2020) 123513. https://doi.org/10.1016/j.cej.2019.123513.
19 T. Wu, J. Kim, J. H. Lim, M. S. Kim, and N. V. Myung: Front. Chem. **9** (2021) 762896. https://doi.org/10.3389/fchem.2021.762896
20 J. H. Kim, S. Y. Back, J. H. Yun, H. S. Lee, and J.-S. Rhyee: Materials **14** (2021) 1564. https://doi.org/10.3390/ma14061564
21 S. A. Yamini, R. Santos, R. Fortulan, A. A. Gazder, A. Malhotra, D. Vashaee, I. Serhiienko, and T. Mori: ACS Appl. Mater. Interfaces **15** (2023) 19220. https://doi.org/10.1021/acsami.3c01956
22 W.-T. Chiu, C.-L. Chen, and Y.-Y. Chen: Sci. Rep. **6** (2016) 23143. https://doi.org/10.1038/srep23143
23 A. M. Dehkordi, M. Zebarjadi, J. He, and T. M. Tritt: Mater. Sci. Eng.: R: Rep. **97** (2015) 1. https://doi.org/10.1016/j.mser.2015.08.001.
24 W. Liu, X. Yan, G. Chen, and Z. Ren: Nano Energy **1** (2012) 42. https://doi.org/10.1038/nmat1821

About the Authors



Yin-Chen Huang received his B.S. degree from National Taiwan Ocean University in 2015, M.S. degree from National Taiwan University in 2017, and Ph.D. degree from Tohoku University in 2024. He is currently an assistant professor at the Institute for Materials Research of Tohoku University. His expertise is in the areas of magnetic material, magetostrictive material, and silicon-based microfabrication. His recent interests cover thermoelectric materials and their applications.



Ping-Chen Lin received his B.S. degree from National Kaohsiung University of Science and Technology, Taiwan, where he is currently studying for his M.S. degree. His research interests are in thermoelectric materials, materials engineering, and sensors.



Tao-Hsing Chen received his B.S. degree from National Cheng Kung University, Taiwan, in 1999 and his M.S. and Ph.D. degrees from the Department of Mechanical Engineering, National Cheng Kung University, in 2001 and 2008, respectively. From August 2008 to July 2010, he was a postdoctoral researcher at the Center for Micro/Nano Science and Technology, National Cheng Kung University. In August 2010, he became an assistant professor at National Kaohsiung University of Applied Sciences (renamed National Kaohsiung University of Science and Technology), Taiwan. Since 2016, he has been a professor at National Kaohsiung University of Science and Technology. His research interests are in metal materials, TCO thin films, thermal sensors, and photosensors. (thchen@nkust.edu.tw)